Structural disjoining potential for grain-boundary premelting and grain coalescence from molecular-dynamics simulations

Saryu J. Fensin,[1] David Olmsted,[2] Dorel Buta,[1] Mark Asta,[1,3] Alain Karma,[2] and J. J. Hoyt[4]

[1]*Department of Chemical Engineering and Materials Science, University of California, Davis, California, 95616 USA*

[2]*Department of Physics and Center for Intersisciplinary Research on Complex Systems, Northeastern University, Boston, Massachusetts, 02115 USA*

[3]*Department of Materials Science and Engineering, University of California, Berkeley, California, 94720 USA*

[4]*Department of Materials Science and Engineering, McMaster University, Hamilton, Ontario, Canada L8S 4L7*

We describe a molecular-dynamics framework for the direct calculation of the short-ranged structural forces underlying grain-boundary premelting and grain coalescence in solidification. The method is applied in a comparative study of (i) a $\Sigma 9 \langle 115 \rangle 120°$ twist and (ii) a $\Sigma 9 \langle 110 \rangle \{411\}$ symmetric tilt boundary in a classical embedded-atom model of elemental Ni. Although both boundaries feature highly disordered structures near the melting point, the nature of the temperature dependence of the width of the disordered regions in these boundaries is qualitatively different. The former boundary displays behavior consistent with a logarithmically diverging premelted layer thickness as the melting temperature is approached from below, while the latter displays behavior featuring a finite grain-boundary width at the melting point. It is demonstrated that both types of behavior can be quantitatively described within a sharp-interface thermodynamic formalism involving a width-dependent interfacial free energy, referred to as the disjoining potential. The disjoining potential for boundary (i) is calculated to display a monotonic exponential dependence on width, while that of boundary (ii) features a weak attractive minimum. The results of this work are discussed in relation to recent simulation and theoretical studies of the thermodynamic forces underlying grain-boundary premelting.

I. INTRODUCTION

At high homologous temperatures the atomic structure of a grain boundary often displays pronounced disorder. In some cases this structural disorder can involve the formation of nanometer-scale intergranular films with liquidlike properties below the bulk melting point, a phenomenon commonly referred to as grain-boundary premelting. The interfacial thermodynamic driving forces underlying grain-boundary premelting are understood to be an important factor influencing grain coalescence behavior during the late stages of solidification (e.g., [1]). Specifically, when premelting is thermodynamically favored there exists an associated repulsive "disjoining pressure" which hinders the coalescence of two misoriented grains at nanometer-scale distances. In such cases a significant undercooling may be required for dendrite arms to merge to form solid "bridges" that are capable of sustaining thermal-contraction stresses without grain sliding or rupture. The quantitative characterization of grain-boundary disjoining forces is thus an important issue in the context of modeling the formation of solidification defects, known as "hot tears," which occur deep within the mushy zone during casting or welding [1–4].

Despite its practical importance in the context of solidification defects, the magnitude and spatial extent of grain-boundary disjoining forces in metals and alloys remain incompletely understood. As in the case of surface premelting [5], these forces can in principle be probed experimentally through measurements of the extent of equilibrium premelting as a function of temperature near the bulk melting point. In comparison to surface premelting, however, the challenges inherent in characterizing the structure of "buried" internal interfaces at high homologous temperatures have significantly limited the number of direct experimental studies of grain-boundary premelting [6–13]. This situation has provided motivation for several recent theoretical studies based on conventional phase-field [14–17] and phase-field-crystal (PFC) [18,19] methods, which have led to new insights into the rich variety of possible premelting behavior that may be exhibited by grain boundaries as a function of their bicrystallography.

Due to the difficulties inherent in validating theoretical models for grain-boundary premelting directly from experimental measurements, the authors recently proposed an independent methodology for calculating grain-boundary disjoining forces from equilibrium molecular-dynamics (MD) simulations [20]. The technique represents an extension of the numerous previous MD studies of grain-boundary premelting performed over the past three decades [21–34]. The technique for calculating disjoining potentials by MD is based on an analysis of the equilibrium distribution of the widths of premelted intergranular films, which are related to the underlying disjoining forces through the fluctuation-dissipation theorem. The purpose of this paper is to describe the technical details surrounding the implementation of this method, and to demonstrate its application in the study of two distinct classes of grain-boundary premelting behavior. Specifically, we consider the premelting behavior of a high and intermediate energy boundary in elemental Ni where the widths of the premelted layers continuously increase or remain finite, respectively, as the melting point is approached from below. It is shown that the former behavior is consistent with a disjoining potential (Ψ) that decreases exponentially with increasing width (w) of the premelted layer, while the

latter behavior can be quantitatively modeled with a dependence of Ψ on w that features a weak attractive minimum at nanometer-scale widths. This minimum is associated with a grain-boundary structure with alternating solid bridges and disordered regions, bearing strong similarities to the type of structure found to be associated with such a minimum in a recent phase-field-crystal study [19].

The remainder of this paper is outlined as follows. In the next section we review a continuum, sharp-interface formalism for the thermodynamic properties underlying grain-boundary premelting and coalescence, based on the definition of the so-called "disjoining potential," the (negative) derivative of which is the disjoining pressure referred to above. Section III discusses the technical details underlying the calculation of the disjoining potential by MD, as well as the details of the simulations undertaken in the current application of the method to the study of high-temperature grain boundaries in fcc Ni. The results are presented in Sec. IV, followed by a summary and discussion of the findings in the context of previous theoretical studies in Sec. V.

II. DISJOINING POTENTIAL

The equilibrium width of a premelted grain boundary in a sharp-interface picture is governed by a competition between bulk and interfacial thermodynamic factors, which can be represented mathematically as follows:

$$G(w) = w\Delta G_f + \Psi(w). \tag{1}$$

In Eq. (1), $G(w)$ represents the total excess free energy of a premelted grain-boundary of width w, which is composed of two contributions: ΔG_f represents the bulk free-energy difference between liquid and solid phases (positive below the melting point), per unit volume, while $\Psi(w)$ represents the disjoining potential. The function $\Psi(w)$ takes the limits of γ_{GB} (the interfacial free energy of a hypothetical "dry" grain boundary) and $2\gamma_{SL}$ (twice the solid-liquid interfacial free energy) for small and infinite values of w, respectively. For intermediate values of the width $\Psi(w)$ can display a complex dependence on w.

The dependence of $\Psi(w)$ on w is generally governed by distinct short and long-ranged contributions. An attractive interaction between solid-liquid interfaces [36,37] arises due to dispersion forces which are dominant at large w, and are predicted to give rise to finite interfacial widths at T_M [36]. For systems where the wetting condition, $\gamma_{GB} > 2\gamma_{SL}$ holds, a repulsive contribution to $\Psi(w)$ arises from short-ranged structural interactions (Ψ_{sr}) associated with the overlap of the density waves in the diffuse regions of the solid-liquid interfaces. Mean-field arguments [38], as well as lattice-gas models (e.g., [28]), yield an exponentially decaying form for this short-ranged contribution,

$$\Psi_{sr}(w) = 2\gamma_{SL} + \Delta\gamma \exp(-w/\delta), \tag{2}$$

where $\Delta\gamma = \gamma_{GB} - 2\gamma_{SL}$ and δ is an interaction length on the order of the atomic spacing. In the absence of long-ranged dispersion forces, insertion of Eq. (2) into Eq. (1) leads to the prediction of an equilibrium grain-boundary width that diverges logarithmically as the melting temperature (T_M) is

approached from below. In previous work [20] we have argued, based on previous estimates of the dispersion forces for surface premelting, that the structural contributions to the disjoining potential for grain-boundary premelting in metals are expected to dominate the long-ranged dispersion contributions for nanometer-scale grain-boundary widths.

Recent theoretical results demonstrate that $\Psi_{sr}(w)$ can generally display more complex dependencies on w than suggested by Eq. (2). Diffuse-interface phase-field models [14–16], which neglect dispersion forces and thus model Ψ_{sr} directly, have shown that depending on grain-boundary misorientation and the detailed choice of interfacial thermodynamic parameters, the premelting transition can exhibit either the continuous behavior associated with Eq. (2), a hysteretic first-order character, or an intermediate behavior where the boundary width increases with increasing temperature but remains finite at T_M (these three types of behavior are referred to as types 2, 1, and 3 in Ref. [34]). The PFC method was recently used to study grain-boundary premelting for both three-dimensional body-centered-cubic (bcc) [18] and two-dimensional hexagonal [19] systems. The latter study involved a systematic investigation of symmetric tilt boundaries as a function of misorientation. Well beyond a critical misorientation angle (where $\gamma_{GB} > 2\gamma_{SL}$) Ψ_{sr} was found to exhibit a purely "repulsive" behavior, monotonically decreasing with increasing w, consistent with Eq. (2). However, well below the critical angle, Ψ_{sr} exhibited an attractive minimum, giving rise to a finite area-averaged liquid-layer width at the melting temperature, reflecting the presence of localized premelting within the cores of the grain-boundary dislocations in low-angle boundaries.

The possibility that the short-ranged contributions to the disjoining potential can exhibit an attractive minimum was considered in earlier theoretical studies of wetting transitions [39]. In these studies a double-exponential ansatz was used to model such behavior. For the purposes of the present study this double-exponential form can be written as follows:

$$\Psi_{sr}(w) = 2\gamma_{SL} + [\Delta_1 \exp(-w/\delta_1) - \Delta_2 \exp(-w/\delta_2)], \tag{3}$$

where Δ_1 and Δ_2, which are both positive quantities, represent the strengths of repulsive and attractive exponential contributions with decay lengths δ_1 and δ_2, respectively. Although Eq. (3) has not been derived directly from a microscopic theory, it provides a useful phenomenological form to model the MD data, as shown below. This equation gives rise to a predicted value of the quantity $\gamma_{GB} - 2\gamma_{SL}$ equal to $\Delta_1 - \Delta_2$, where again γ_{GB} is the interfacial free energy of a hypothetical dry grain boundary given by the limit of w going to zero in Eq. (3). Choosing $\delta_2 > \delta_1$, and if $\Delta_1 > \Delta_2$, as in the results given below, this disjoining potential is repulsive at short distances, attractive at large w, and features a minimum at a width w_m given as

$$w_m = \frac{\delta_1\delta_2}{\delta_2 - \delta_1} \ln\left[\frac{\Delta_1\delta_2}{\Delta_2\delta_1}\right]. \tag{4}$$

With the form for the disjoining potential given by Eq. (3) the width of the premelted boundary is predicted to be finite, with a value w_m, at the melting point.

TABLE I. The grain-boundary types used in the MD simulations along with the simulation cell sizes, reported at zero temperature. For reference the lattice constant of FBD Ni potential at zero temperature is 3.52 Å. These boundaries span a large range of $\gamma_{GB}^0/2\gamma_{SL}$, where γ_{GB}^0 is the zero-temperature grain-boundary energy, and γ_{SL} is the solid-liquid interfacial free energy.

Grain-boundary type	L_x (Å)	L_y (Å)	L_z (Å)	γ_{GB}^0 (mJ/m²)	$\gamma_{GB}^0/2\gamma_{SL}$
$\Sigma9\langle011\rangle\{411\}38.9°$ symmetric tilt	237.86	32.36	31.68	909	1.5
$\Sigma9\langle115\rangle120°$ twist	253.23	37.34	38.80	1440	2.5
$\Sigma11\langle011\rangle\{311\}50.5°$ symmetric tilt	246.55	32.36	33.02	450	0.79

In the MD results presented below we demonstrate the disordering behavior for two grain boundaries with relatively high and intermediate energies which we show can be quantitatively modeled by Eqs. (2) and (3), respectively. To compute quantitative values for the disjoining potentials from these simulations, we make use of the following relation between $G(w)$ and the equilibrium distribution $P(w)$ of grain-boundary widths sampled by the MD systems at a temperature T: $P(w) \propto \exp[-AG(w)/k_B T]$, where A is the interfacial area. Calculations of $P(w)$ by MD, combined with an accurate knowledge of the bulk melting properties underlying ΔG_f allows one to extract $\Psi(w)$, as described below. Since the MD simulations are based on a short-ranged classical interatomic-potential model, they do not include the long-ranged dispersion-force contributions to $\Psi(w)$, and thus sample $\Psi_{sr}(w)$ directly.

III. METHODOLOGY

In this study the simulations were based on an embedded-atom method (EAM) interatomic-potential model for Ni developed by Foiles, Baskes and Daw (FBD) [40]. This potential was chosen as we have in previous work characterized both the bulk melting properties and solid-liquid interfacial free energies for FBD Ni; both sets of properties are prerequisites for a quantitative study of grain-boundary premelting. As reviewed in Ref. [20] the melting temperature for the FBD Ni potential has been bracketed to lie in the range $T_M = 1709-1710$ K, and the value of the solid-liquid interfacial free energy has been calculated to be $\gamma_{SL} = 285$ mJ/m² [41]. The latent heat for the potential was also calculated to be 0.015 eV/Å³.

In the present study we considered the following three different grain-boundary structures: a $\Sigma9$ symmetric $\langle011\rangle\{411\}38.9°$ tilt boundary (hereafter referred to as the $\Sigma9$ tilt boundary), a $\Sigma11$ symmetric $\langle011\rangle\{311\}50.5°$ tilt boundary (hereafter referred to as the $\Sigma11$ tilt boundary), and a $\Sigma9\langle115\rangle120°$ twist boundary (hereafter referred to for convenience as the $\Sigma9$ twist boundary, even though we recognize that this boundary can also be described as a symmetric tilt boundary). These were selected from a large library of grain-boundary structures that fit into moderately sized periodic simulation cells, developed in the work of Olmsted *et al.* [42]. As shown in Table I, the selected boundaries have zero-temperature energies (γ_{GB}^0) that span a range of values relative to $2\gamma_{SL}$, and were thus expected to feature a range of premelting behavior.

A. Energy minimization

The optimization of grain-boundary structures at zero temperature made use of a simulation block with two grains separated by a flat grain boundary as shown in Fig. 1.

The cell was periodic in the plane of the boundary and nonperiodic perpendicular to it. The grains were sandwiched between two slabs parallel to the grain-boundary plane. The atoms in each of these slabs were fixed relative to each other and could only undergo a rigid body motion. The slabs could move normal to the boundary, allowing volume expansion to maintain zero normal stress, and in the plane of the boundary, avoiding any resistance from the surfaces to translational movement of the grains relative to each other. Multiple trial configurations were built in order to minimize the boundary energy with respect to relative translations of the grains and with respect to the number of atoms in the grain boundary, as described in Ref. [42]. The energy of each trial configuration was minimized using the conjugate gradient method. After minimization, the energy of the grain boundary was computed as the total energy of the unconstrained atoms, less the bulk crystal energy for the same number of atoms, divided by the area of the boundary. The dimensions of the computational cell used in these energy minimizations and in the subsequent MD simulations are given in Table I.

B. Molecular-dynamics simulations

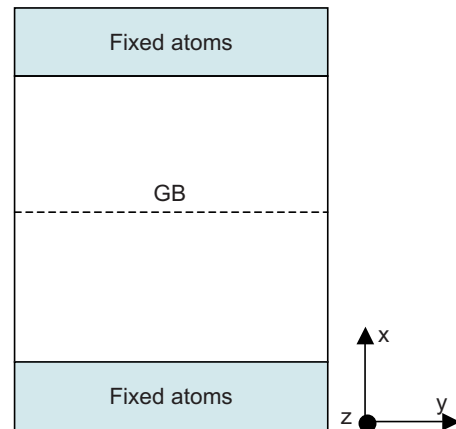Finite temperature simulations were performed by MD employing the LAMMPS code [43]. All simulations were per-

FIG. 1. (Color online) Computational cell used for molecular-dynamics simulations at zero temperature. The boundary plane is in the y-z directions. The cell is periodic in y and z.

formed with a constant number of atoms, constant volume, and temperature (*NVT* ensemble). The temperature was maintained by using a Nose-Hoover thermostat [44] with a thermostat relaxation time of 0.1 ps, employing a time-step of 1 fs. The simulations began with the optimized zero-temperature geometry, which was equilibrated at different temperatures. Prior to each simulation at a given temperature, the periodic lengths parallel to the grain-boundary plane were expanded according to the finite-temperature value of the lattice constant for the bulk crystal (determined separately). These periodic lengths were then held constant in all of the *NVT* MD simulations. The atoms in the slabs that were held fixed during the energy minimization procedure were made dynamic for the finite-temperature simulations, and the boundary conditions were modified such that both the grains terminated in free surfaces.

As discussed in the next subsection, two types of analysis were conducted on the simulated systems to study their pre-melting behavior. The first was a calculation of the excess volume as a function of temperature. In the simulations used for this analysis equilibration times were a few ns. The system volume was sampled over a total time of at least 10 ns at a frequency of 10 ps.

The second analysis involved the calculation of equilibrium grain-boundary-width histograms. For these analyses, the simulations started at a given temperature with an equilibration lasting 10 ns. Statistics were then obtained for the boundary width histograms from a total of 4000 snapshots, sampled at a frequency of 10 ps. As discussed below, this number of snapshots and sampling rate ensured that at least a hundred statistically independent samples were obtained at each of the temperatures studied for the histogram analysis.

C. Calculation of excess volume and width histograms

Prior to performing detailed analyses of width histograms, we performed an analysis of premelting behavior based on the temperature dependence of the excess volume. The excess volume was calculated by time averaging over values for single configurations, computed as follows. For a single snapshot the excess volume was computed from the distance between two lattice planes, one in each grain. These planes were chosen in each grain such that they were far from the boundary and the free surfaces. The volume of material that would lie between the two planes in a perfect crystal can be computed by counting the total number of atoms between the two planes (including half of the atoms in each of the two planes) and multiplying that number by the volume per atom of the bulk crystal at the same temperature (and zero pressure). The difference between the actual volume and the expected bulk volume, divided by the area of the boundary, is the excess volume. A slight linear dependence of this measured excess volume on the distance between the planes was found, presumably the result of the numerical error in the lattice constant at high temperature. However, any consistent choice was adequate for our purposes here, as the excess volume results were used mainly to determine the qualitative nature of the premelting behavior, as discussed below. The specific planes chosen for the excess volume were 1/4 and 3/4 of the way through the simulation cell.
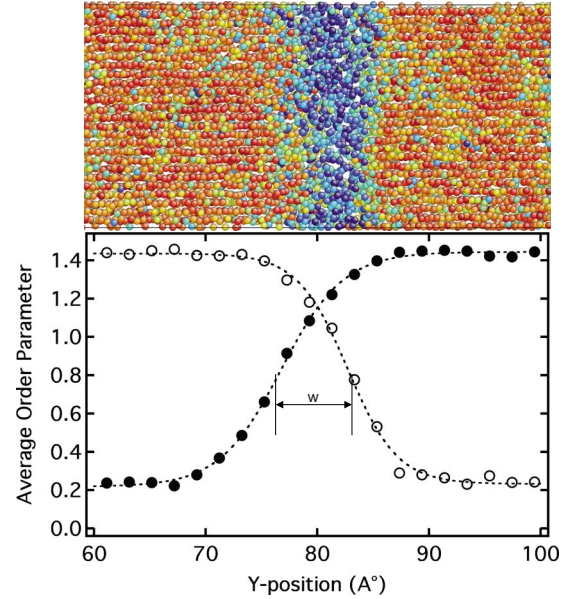

FIG. 2. (Color online) A snapshot of a premelted grain boundary at an undercooling of 2 K and the corresponding average order parameter versus distance across the grain boundary. Atoms in the top panel are colored based on the order-parameter value with lighter color (red in the online figure) representing atoms in either of the two grains and darker color (blue in the online figure) showing atoms in the grain boundary. The construction used to determine the grain-boundary width w is illustrated in the bottom panel and a width of $w \approx 13.5$ Å is obtained.

In order to compute equilibrium grain-boundary-width distributions, $P(w, T_i)$, for a given interface temperature T_i, we proceeded as follows. For each snapshot the grain-boundary width w was determined using a scheme developed by Hoyt *et al.* [41] for the analysis of solid-liquid interface capillary fluctuations. In this approach each atom is assigned a structural order parameter, $\phi_i = \frac{1}{12}\Sigma_j|\vec{r}_{ij} - \vec{r}_{ij}^c|^2$, where r_{ij} are the actual positions of the 12 nearest neighbors of atom i and r_{ij}^c are the atom sites for the corresponding neighbors for the solid phase in the perfect crystal. The ϕ_i values are then averaged in bins along the direction normal to the boundary and the point of inflection in the average order-parameter profile is taken as the position of the grain boundary. In the case of grain boundaries two separate profiles are required. The first uses r_{ij}^c for the crystal orientation of one of the two grains in the bicrystal, and for the second r_{ij}^c is chosen based on the other grain. After these two order-parameter profiles (ϕ_1 and ϕ_2) are obtained each is fit to the following function:

$$\phi(x) = a + b \tanh[(x - x_0)/d], \quad (5)$$

where a, b, x_0, and d are fitting parameters, and the boundary width is derived from the difference in values of x_0 determined from the ϕ_1 and ϕ_2 profiles.

The analysis used to compute grain-boundary widths is illustrated graphically in Fig. 2 for a snapshot of the $\Sigma 9$ twist boundary at an undercooling of 2 K below the bulk melting temperature. In Fig. 2 the top panel shows the atoms, color coded according to the magnitude of the difference in the

order-parameter values, lighter colors (red in the on-line figure) denoting atoms in an environment corresponding to either of the two grains, and darker colors (blue in the on-line figure) indicating an environment that does not correspond to either grain. The corresponding order-parameter profiles with the fits to Eq. (5) (solid lines) are shown in the bottom of Fig. 2. The width is defined as the difference in the center positions of the fits to ϕ_1 and ϕ_2. In this example, a width of 13.5 Å is obtained by the analysis. We note that the width of the boundary in this example is comparable to the intrinsic width of the order-parameter profile, so that the diffuse "solid-liquid" interfaces on either side of the boundary are clearly overlapping. This overlap leads to interactions between the interfaces which are quantitatively described by the disjoining potential.

It should be emphasized that the choice of an order parameter used to compute the grain-boundary width is not unique (this point was discussed also in a recent related study by Williams and Mishin [33]). Other choices for the structural order parameter used to define an interface width would include the so-called centrosymmetry parameter [45], the order parameter used by Morris in studies of solid-liquid interfaces [46], excess mass used by Mellenthin *et al.*[19], a parameter introduced by Williams and Mishin [33] based on the local structure factor, and an order parameter introduced by von Alfthan *et al.* [34] based on structural units. Different choices for the order parameter are expected to lead to slightly different values for the interface width, and the quantitative values of the disjoining potential derived from them. For example, in the sharp-interface formalism we describe the limit of $\Psi(w)$ for small w as the interfacial free energy of a hypothetical "dry" grain boundary—we would expect that this limiting value will depend on the way in which the width is defined, which is not unreasonable since with any choice of this definition a real boundary at zero temperature will have some small finite width. The ambiguities associated with the different choices for the definition of width are inherent in the use of a sharp-interface theoretical formalism to describe the properties of systems such as these with diffuse interfaces. In applications of such sharp-interface models, however, the ambiguity presents no problem in practice provided that each of the bulk and interfacial thermodynamic quantities is defined consistently.

In order to determine whether the simulation times employed in this study were sufficient to give adequate statistics for the width histograms, we estimated the correlation time for width fluctuations based on an analysis of the decay of a width autocorrelation function $C(\Delta t)$ defined as follows:

$$C(\Delta t) = \langle w(t)w(t + \Delta t)\rangle - \langle w\rangle^2, \qquad (6)$$

In Eq. (6), $w(t)$ denotes the instantaneous width of the grain boundary at a time t, and $\langle \ldots \rangle$ denotes ensemble (time) averages. The time required for the autocorrelation function to decay by a fraction of $1/e$ was taken as a measure of the correlation time.

The correlation times were found to vary significantly with boundary type and temperature. The maximum value of the correlation time was obtained as 100 ps for the $\Sigma 9$ tilt boundary at a temperature 2 K below T_M. Given that 4000

snapshots were sampled in the MD simulations, at a frequency of 10 ps, at least a hundred independent samples were obtained for each of the histograms presented below.

D. Calculation of disjoining potentials from width histograms

As discussed in the previous section, the probability of observing a given boundary width at an interface temperature T_i is related to the total free energy of the system as follows:

$$P(w,T_i) = C_i \exp[-A_i G(w,T_i)/k_B T_i], \qquad (7)$$

where A_i is the area and $G(w,T_i)$ is given by Eq. (1). In the above expression the subscript i denotes one of the seven different temperatures for which the width histograms have been calculated by MD: $T_1 = 1710$, $T_2 = 1708$, $T_3 = 1705$, $T_4 = 1700$, $T_5 = 1690$, $T_6 = 1680$, $T_7 = 1650$ K, which represent undercoolings relative to the bulk melting temperature, $T_M = 1710$ K, ranging between zero and 60 K. Equation (7) emphasizes the fact that each undercooling yields a histogram that spans a different range of widths, and the unknown normalization constants at each temperature are denoted as C_i.

As discussed in the next section, analyses of the calculated width histograms were undertaken to compute disjoining potentials for two different boundaries, one of which (the $\Sigma 9$ twist) featured a diverging interface width as T_M is approach from below, and another (the $\Sigma 9$ tilt) whose width remains finite at T_M. In the former case the disjoining potential was modeled using the form given by Eq. (2), while for the latter use was made of Eq. (3). The unknown parameters in these expressions can be obtained in two ways based on the MD-calculated width histograms using Eq. (7). The first is to fit the histogram data at each temperature independently. This gives a range of values for the disjoining-potential parameters, which are expected to be more accurate at the higher temperatures where one has access to the largest range of width values. A refined estimate of the potential parameters can be obtained from a histogram analysis using all of the data at once, as follows.

From Eq. (1) the disjoining potential can be written as

$$\Psi(w) = G(w,T_i) - w\Delta G_f(T_i), \qquad (8)$$

where ΔG_f is the bulk free-energy difference between liquid and solid per unit volume. For the EAM Ni system studied here the temperature dependence of ΔG_f is known accurately from previous studies. For the small range of temperatures considered in the MD simulations of width histograms, which are close to the bulk melting temperature, ΔG_f can be accurately computed from the following expression:

$$\Delta G_f = (\Delta T_i/T_M)L, \qquad (9)$$

where L is the latent heat per unit volume, and $\Delta T_i = T_M - T_i$ is the interface undercooling. From Eq. (7), the disjoining potential can be written in terms of the equilibrium width distribution as

$$\Psi(w) = -k_B T_i[\ln P(w,T_i)]/A_i - w\Delta G_f + a_i, \qquad (10)$$

where the a_i are unknown constants related to C_i in Eq. (7). These parameters lead to constant offsets when the quantity

$-k_B T_i[\ln P(w, T_i)]/A_i - w\Delta G_f$ is plotted versus w for each interface temperature. To construct the disjoining potential a least-squares fit is used to refine the values of the shift parameters (a_i) along with the potential parameters [$\Delta\gamma$ and δ in Eq. (2) or Δ_1, δ_1, Δ_2, and δ_2 in Eq. (3)]. In this procedure the initial values for the shift parameters were estimated "by eyes" to give maximal overlap between the data, and the initial values for the potential parameters were obtained from an average of the independent fits to the data at separate temperatures (described above). The values of the parameters were then iteratively refined to minimize the square of the differences between the MD data and the analytical expressions for $\Psi(w)$.

E. Effects of thermostat, system size, and boundary conditions

In the course of this work additional studies were also conducted to investigate the effects of the details of the simulation methodology on the resulting disjoining potentials. These additional analyses were performed for the $\Sigma 9$ twist boundary in Ni as well as a series of $\langle 100\rangle$ tilt boundaries in Ni and bcc Fe. An EAM potential developed by Mendelev *et al.* [35] was used for bcc Fe.

The first issue addressed in these additional simulations was the effect of thermostat. Equation (7) assumes that the measured grain-boundary widths sample a canonical ensemble, and in order to achieve this by MD simulations we employed a standard Nose-Hoover thermostat [44] in the present work. An alternative choice would be to use a Langevin thermostat [47], which would relax temperature fluctuations faster locally and produce different dynamics in the system, but would be intended to sample the same ensemble. To test for unexpected effects of dynamics on the equilibrium width histograms and disjoining potential, two boundaries showing continuous premelting behavior (i.e., diverging widths as the melting temperature is approached from below), one in bcc Fe and one in fcc Ni, were simulated using both a Nose-Hoover thermostat and a Langevin thermostat with a time constant of 0.25 ps. No statistically significant differences in the disjoining potential were found with the two thermostats. Further, we tested a range of reasonable time constants for both thermostats, finding that statistically significant effects on the calculated disjoining potentials were again absent unless the relaxation time for the Langevin thermostat was reduced to extremely short time scales, on the order of the inverse of the vibrational frequencies in the system. Interestingly, in simulations which used the same time constant of 0.25 ps, the correlation time for width fluctuations was found to be substantially reduced in the simulations with the Langevin relative to those with the Nose-Hoover thermostat. The Langevin thermostat thus offers the potential advantage of providing improved statistics related to width histograms for a given simulation time.

The second issue investigated was the effect of system size on the calculated disjoining potential. For atomically rough grain boundaries, such as those investigated in this work, previous theoretical studies have demonstrated that capillary fluctuations should give rise to a weak dependence of the disjoining potential on cross-sectional area [14,28]. To
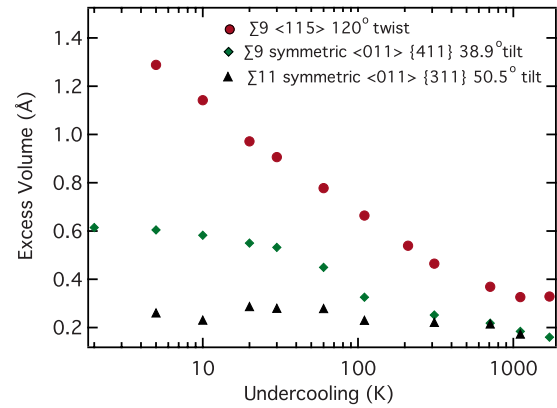

FIG. 3. (Color online) Excess volume versus temperature plot for three different grain boundaries in Nickel. The red circles correspond to a $\Sigma 9\langle 115\rangle$ twist grain boundary, the green diamonds correspond to a $\Sigma 9$ symmetric $\langle 011\rangle\{411\}$ tilt grain boundary and the black triangles correspond to a $\Sigma 11$ symmetric $\langle 011\rangle\{311\}$ tilt grain boundary.

check for any unexpected large system-size effects, simulations were performed for the $\Sigma 9$ twist boundary using both the cross-sectional area given in Table I, as well as an area that was four times larger (i.e., with periodic lengths that were doubled in each of directions parallel to the boundary). Although the width histograms obtained for the larger system were much narrower, as expected from Eq. (7), it was still possible to obtain data over a sufficiently large range of widths to extract a disjoining potential. The results for the disjoining potential were found to be consistent with those obtained from the smaller system provided that a small effect of system size on the bulk melting temperature (amounting to a roughly one-degree lowering of T_M for the larger system, which is within the accuracy of the known value of the bulk melting point) was accounted for in the analysis. Similar results were obtained in analyses of system-size effects on calculated disjoining potential for a high-energy $\langle 100\rangle$ tilt boundary in Ni.

A final issue that was investigated in these studies concerns the effect of boundary conditions on the calculated width distributions. For a high-angle $\langle 100\rangle$ symmetric tilt boundary in Fe this was investigated by computing width distributions at 10 K undercooling using both the free-surface boundary conditions employed in the current study, as well as a full periodic boundary condition in a simulation cell containing two grain boundaries and a periodic length normal to the boundaries that was allowed to be dynamic to maintain zero normal stress. No statistically significant differences were found between the width distributions derived with the two different boundary conditions.

IV. RESULTS

The effect of temperature on the structure of the three boundaries considered in this work is illustrated in Figs. 3 and 4. Figure 3 plots the calculated excess volume versus the logarithm of the interface undercooling, and displays three qualitatively different types of behavior. The $\Sigma 9$ twist bound-
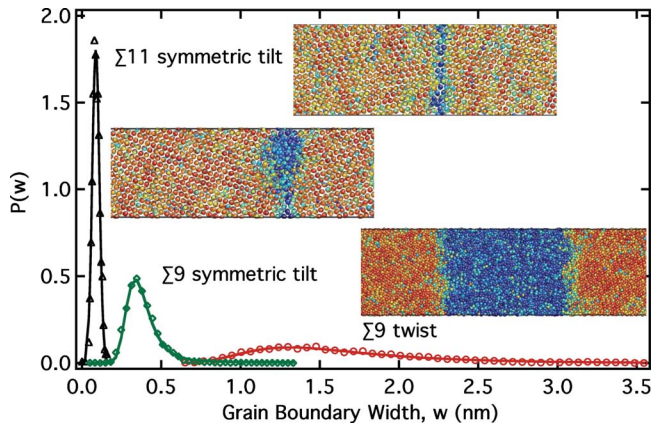
FIG. 4. (Color online) The distribution function $P(w)$ vs w from the MD simulations for the three different boundaries at 1708 K. The green diamonds and the red circles correspond to the $\Sigma9$ tilt and twist grain boundaries respectively. The $\Sigma11$ tilt boundary is represented by the black triangles. The lines represent a least square fit of the premelting models of Eqs. (1) and (2) for the $\Sigma9$ twist grain boundary, Eqs. (1) and (3) for the $\Sigma9$ tilt boundary and a Gaussian fit for the $\Sigma11$ tilt boundary. The snapshots next to each figure correspond to the widest grain boundary for each boundary and are color coded according to the ϕ_i values. Lighter color (red in the online figure) indicates an atom with an environment corresponding to one of the two grains, darker color (blue in the on-line figure) represents atoms in some other environment.

ary has an excess volume (represented by the red circles) that continuously increases as the melting temperature is approached from below. The behavior displayed by this boundary in Fig. 3 is consistent with a logarithmic divergence of the interface width, as would be expected if the disjoining potential is of the form given by Eq. (2). At the opposite extreme, the $\Sigma11$ tilt boundary (represented by the black triangles) has an excess volume that is relatively small and depends only weakly on temperature. The $\Sigma9$ tilt boundary (represented by the green diamonds) displays an intermediate behavior. The excess volume increases sharply between 300 K undercooling and 30 K undercooling. At high temperature, the rate of increase in the excess volume decreases and the boundary maintains a finite excess volume at T_M.

Representative snapshots and calculated width histograms are shown in Fig. 4 for each of the three boundaries at 1708 K (two degrees below T_M). The width histogram corresponding to the $\Sigma9$ twist boundary is much broader than those for the other two boundaries. This boundary samples relatively large widths, and $P(w)$ shows pronounced asymmetry with an extended tail to large w values. The $\Sigma11$ tilt boundary, by contrast, features a width histogram that is very narrow and is centered on relatively small values of w. The width distribution for this boundary is more symmetric than those for the $\Sigma9$ twist and tilt boundaries. The width distribution for the $\Sigma9$ tilt boundary shows features intermediate between the other two. The average width is larger than that of the $\Sigma11$ boundary, and the width distribution is considerably broader. Compared to the $\Sigma9$ twist boundary, however, the asymmetry and the tail extending to larger widths is not nearly as pronounced in the width distribution for the $\Sigma9$ tilt boundary.
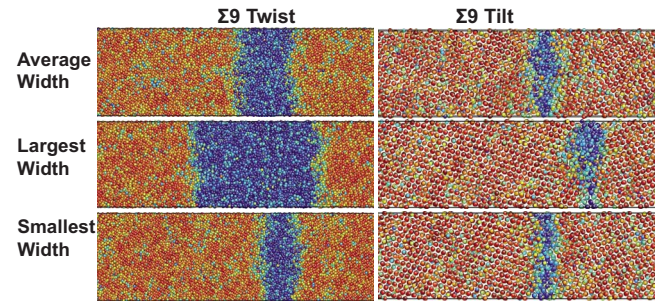

FIG. 5. (Color online) Snapshots from a MD simulation at an undercooling 2 K illustrating the dynamic nature of the grain-boundary width. The snapshots corresponding to the $\Sigma9$ tilt grain boundary are on the right of the panel. The snapshots to the left are from the $\Sigma9$ twist boundary discussed elsewhere [20]. The atoms are colored by the difference between the two order parameters as described above.

The MD snapshots in Fig. 4 next to each histogram provide additional insights into the nature of the high-temperature structural disorder present in each of the three boundaries. As in Fig. 2, the atoms in these snapshots have been colored based on the difference between values of the structural order parameters (ϕ_1 and ϕ_2) defined above. Lighter colors (red in the online figure) indicate atoms with an environment corresponding to one of the two grains, while darker color (blue in the online figure) denotes a disordered environment distinct from those in either of the grains. The snapshots and width histograms show that the $\Sigma9$ twist boundary at 1708 K displays thick premelted layers, consistent with the continuous premelting behavior suggested by the excess volume. The $\Sigma11$ tilt boundary is seen to display appreciable disorder only over a width that is on the scale of one atomic plane; this boundary is observed in the MD simulations to remain highly ordered up to T_M. The intermediate behavior of the $\Sigma9$ tilt boundary is characterized by disorder that extends over a distance of several atomic planes. An important feature of the disorder observed in this boundary is the nonuniform character of the widths along the area of the boundary. As illustrated in the snapshot of this boundary in Fig. 4, thick and extended regions of disorder up to a nanometer or more in thickness are often observed in part of the boundary, with much narrower, more ordered regions in between. For the remainder of this section we will focus on the behavior of the two $\Sigma9$ boundaries, showing that the temperature dependence of the width histograms can be accurately described by the disjoining-potential formalism described above.

Figure 5 further illustrates the nature of the disorder present in the $\Sigma9$ twist and tilt boundaries. The snapshots were obtained from a 40 ns MD simulation at 1708 K, and represent the largest, smallest and an average value for the interface widths. Results for the $\Sigma9$ twist boundary are shown on the left and those for the $\Sigma9$ tilt boundary are on the right of Fig. 5. The snapshots illustrate the highly dynamic nature of the boundary structures at 1708 K. The large fluctuations in interface width displayed by these boundaries forms the basis for the histogram analysis underlying calculations of the disjoining potential.
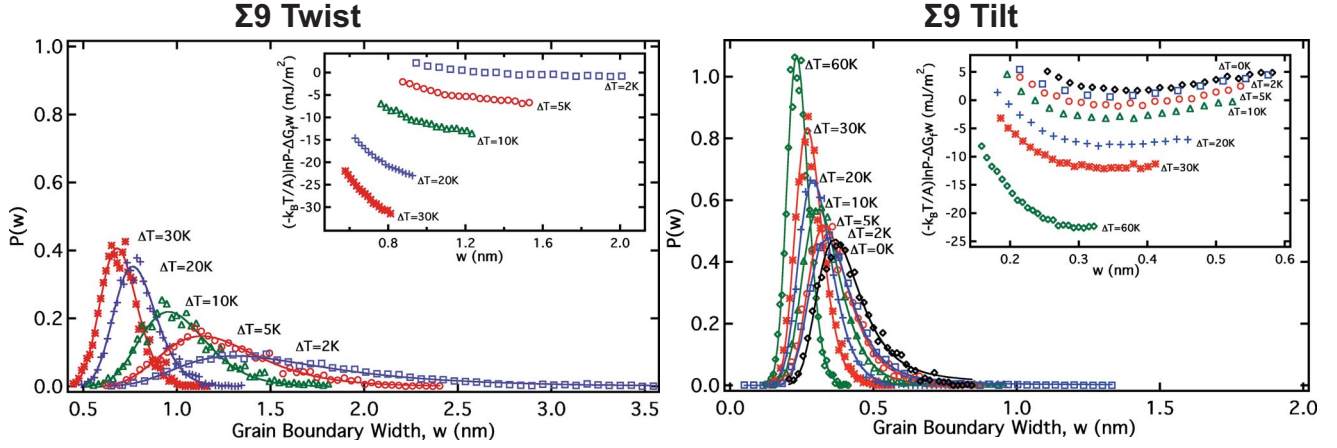
FIG. 6. (Color online) The distribution function $P(w)$ vs w from the MD simulations. The function corresponding to the $\Sigma 9$ tilt grain boundary is in the right of the panel. The function to the left is from the $\Sigma 9$ twist boundary discussed elsewhere [20]. The lines represent least square fits of the premelting model of Eqs. (1) and (2) for the $\Sigma 9$ twist grain boundary and Eqs. (1) and (3) for the $\Sigma 9$ tilt boundary.

The calculated width histograms for both $\Sigma 9$ boundaries are displayed over a range of interface undercoolings in Fig. 6. The histograms on the left and right in Fig. 6 correspond to the $\Sigma 9$ twist and tilt boundaries, respectively. For both of the boundaries the histograms become broader as the bulk melting temperature is approached (i.e., with decreasing undercooling). For the $\Sigma 9$ twist boundary the system is observed to melt completely over the course of the MD runs at the bulk melting temperature, and histograms can be obtained for this boundary only for finite values of the undercooling. By contrast, the width of the $\Sigma 9$ tilt boundary remains finite at T_M over the time scale of the MD runs, consistent with the presence of a free-energy barrier that keeps the system from uniformly melting during the simulations. As a consequence, the width histogram can be calculated at zero undercooling for this boundary, as shown in Fig. 6. The inset in each of the panels shows the quantity $-k_B T_i [\ln P(w, T_i)]/A_i - w\Delta G_f$ versus w for all of the interface temperatures. The data for the $\Sigma 9$ tilt boundary show clear evidence of an attractive minimum in the disjoining potential, as will be discussed further below.

The solid lines in Fig. 6 represent the least square fits of the MD data for $P(w)$ to the disjoining-potential formulas given by Eqs. (7), (1), and (2) for the $\Sigma 9$ twist boundary, and Eqs. (7), (1), and (3) for the $\Sigma 9$ tilt boundary. For the $\Sigma 9$ twist boundary the potential parameters obtained from the separate fits to the data for the individual temperatures span the range $\delta = 0.25$ to 0.29 nm, and $\Delta\gamma = 101$ to 150 mJ/m^2. For the $\Sigma 9$ tilt boundary the fitted values for δ_1 and δ_2 ranged between 0.142–0.144 nm and 0.143–0.144 nm, respectively, $\Delta_1 - \Delta_2$ spanned the values 103 to 163 mJ/m^2, and Δ_2/Δ_1 took values between 1.003 and 1.006. With these fitted potential parameters, the disjoining potential for the $\Sigma 9$ tilt boundary exhibits a weak minimum at a width w_m with values ranging between 0.32 and 0.36 nm, and a depth relative to $2\gamma_{SL}$ varying between -7 and -11 mJ/m^2. The fact that the MD calculated width histograms can be accurately described by disjoining potentials with a relatively narrow range of fitted potential parameter values indicates that the formalism described in the previous section represents a

valid model for describing the temperature dependence of the structural disorder observed in these boundaries.

In order to refine the calculation of the disjoining potential for the $\Sigma 9$ twist and tilt boundaries, we employ the histogram analysis described in the previous section, involving a refinement of both the shift parameters a_i and the potential parameters in Eqs. (2) and (3) for the twist and tilt boundaries, respectively. The resulting fits are shown in Fig. 7 and correspond to the following values for the potential parameters: $\delta = 0.25$ nm and $\Delta\gamma = 156$ mJ/m^2 for the $\Sigma 9$ twist boundary, and $\Delta_1 - \Delta_2 = 103$ mJ/m^2, $\Delta_2/\Delta_1 = 1.003$, $\delta_1 = 0.1471$ nm, $\delta_2 = 0.1474$ nm for the $\Sigma 9$ tilt boundary. These parameter values are consistent with the values given above from the independent fits. The excellent agreement of the fits with the MD data in Fig. 7 again indicates that the disjoining-potential formalism represents an accurate framework for modeling the premelting behavior of these $\Sigma 9$ boundaries. The analysis used to obtain the results of fits in
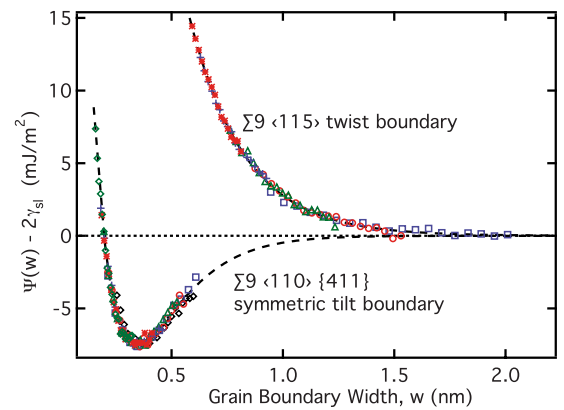

FIG. 7. (Color online) An illustration of the histogram method used to extract the disjoining potential. It shows the merged data from individual histogram data used to reproduce the complete disjoining potential $\Psi(w)$ for the $\Sigma 9$ twist and the $\Sigma 9$ tilt boundaries. The solid line is the best fit to the exponential decay given in Eq. (2) for the $\Sigma 9$ twist boundary, and the dashed line represents the best fit to the double-exponential function in Eq. (3) for the $\Sigma 9$ tilt grain boundary.

Fig. 6 assumed a melting point of $T_M = 1710$ K. If the melting temperature is changed even by one degree, i.e., $T_M = 1709$ K then poor fits to $P(w)$ are obtained for the data at the lowest undercoolings.

The calculated disjoining potentials in Fig. 7 are characterized by the following features. For the $\Sigma 9$ tilt boundary the disjoining potential has a minimum at a finite width, w_m, which corresponds to the average equilibrium grain-boundary width at the melting temperature. The potential is repulsive for $w < w_m$ and attractive for $w > w_m$. In contrast, the $\Sigma 9$ twist boundary features a purely repulsive disjoining potential that is well modeled by the exponential form given in Eq. (2), as expected based on the logarithmic divergence of the excess volume calculated for this boundary (see Fig. 3).

V. SUMMARY AND DISCUSSION

In this paper we have presented a detailed description of a method for computing the disjoining potential for grain-boundary premelting and grain coalescence from an analysis of width fluctuations measured in equilibrium MD simulations. The approach has been applied to two grain boundaries in an EAM model of elemental Ni. For the $\Sigma 9$ twist boundary, which features an excess volume that increases logarithmically as T_M is approached from below, the measured width histograms are consistent with a disjoining potential that decays exponentially, with a decay length of approximately 0.25 nm and a maximum value at zero width of approximately 160 mJ/m^2 relative to $2\gamma_{SL}$. For the $\Sigma 9$ tilt boundary, which features an excess volume that remains finite at T_M, the measured width histograms are shown to be consistent with a disjoining potential that features a weak attractive minimum at $w_m \approx 0.34$ nm, with a depth relative to $2\gamma_{SL}$ of approximately -8 mJ/m^2.

It is interesting to compare the results of the present work with previous studies of grain-boundary premelting based on MD simulations, phase-field theory and PFC calculations. The exponential form of the disjoining potential for the $\Sigma 9$ twist boundary presented here and in Ref. [20] is qualitatively consistent with the results of previous investigations where a diverging grain-boundary width has been observed for high-energy boundaries in a variety of different systems (e.g., [25,26,28,34]). The disjoining potential calculated here for the $\Sigma 9$ tilt boundary features a weak attractive minimum at w_m, and is repulsive and attractive for smaller and larger values of w, respectively. This form for the disjoining potential corresponds to a grain boundary whose width increases with T at low temperature, but remains finite at and above T_M (up to some maximum superheating). This type of behavior for the temperature dependence of the grain-boundary width is qualitatively similar to that found in recent MD studies for one of three twist boundaries in Si [34] and a symmetric tilt boundary in Cu [33].

As discussed in the Introduction section disjoining potentials with attractive minima, qualitatively similar to that calculated here for the $\Sigma 9$ tilt boundary, were obtained in PFC calculations by Mellenthin *et al.* [19] for low-angle tilt boundaries in a model two-dimensional hexagonal system.
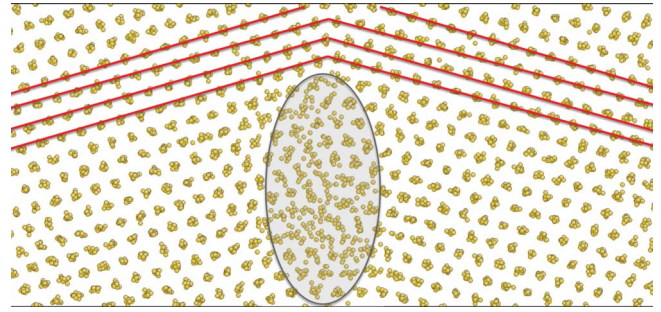

FIG. 8. (Color online) Snapshot of the $\Sigma 9$ tilt boundary at 1708 showing the nonuniform structural disorder in the grain boundary. The gray ellipse shows the regions with high disorder while the red lines highlight the ordered bridges.

The boundaries which displayed this type of disjoining potential had highly nonuniform interface structures, containing premelted regions localized on grain-boundary dislocation cores and separated by well ordered regions which we will refer to as solid "bridges." For these structures, the width corresponding to the minimum in the disjoining potential, which represents an average over the area of the boundary, corresponds to the thickness of an equivalent uniform layer with the same amount of "liquid" as contained in the premelted cores. This area-averaged width can be quite small (e.g., on the order of the atomic spacing) even though the radius of the premelted cores is much larger.

It is interesting to compare the structures observed in the PFC calculations of Mellenthin *et al.* [19] with those for the $\Sigma 9$ tilt boundary considered in the present study. Visual inspection of the numerous snapshots showed that the disorder in this boundary is indeed often highly nonuniform, as illustrated in Fig. 8. This figure shows a representative snapshot from a simulation at $T = 1708$ K, viewed down the tilt axis. In Fig. 8, the structural disorder in the boundary is clearly nonuniform-the region of high structural disorder is highlighted by the gray ellipse, while the red lines connected across the boundary plane highlight the ordered solid bridges. Thus, even though the $\Sigma 9$ boundary studied in the present work has a misorientation angle (38.9°) which is far too large for its structure to be described in terms of separated grain-boundary dislocation cores, the nonuniform nature of the structural disorder and the presence of solid "bridges" is qualitatively very similar to the types of structures observed in Ref. [19].

It should be emphasized, however, that the structure of the $\Sigma 9$ tilt boundary observed in the MD simulations is highly dynamic (cf., Fig. 5) such that the solid bridges form and disappear rapidly on the time scale of the simulations. This behavior could have interesting consequences for the shear response of such boundaries, as the solid bridges are expected to offer enhanced resistance to shear which would otherwise be expected to be very limited for a premelted grain boundary (e.g., [26]). The shear response of such boundaries would thus be an interesting topic for future MD studies.

[1] M. Rappaz, A. Jacot, and W. J. Boettinger, Metall. Mater. Trans. A **34**, 467 (2003).

[2] M. Rappaz, J. M. Drezet, and M. Gremaud, Metall. Mater. Trans. A **30**, 449 (1999).

[3] N. Wang, S. Mokadem, M. Rappaz, and W. Kurz, Acta Mater. **52**, 3173 (2004).

[4] M. Asta, C. Beckermann, A. Karma, W. Kurz, R. Napolitano, M. Plapp, G. Purdy, M. Rappaz, and R. Trivedi, Acta Mater. **57**, 941 (2009).

[5] J. G. Dash, H. Fu, and J.-S. Wettlaufer, Rep. Prog. Phys. **58**, 115 (1995).

[6] R. W. Balluffi and R. Maurer, Scr. Metall. **22**, 709 (1988).

[7] R. A. Masumura, M. E. Glicksman, and C. L. Vold, Scr. Metall. **6**, 943 (1972).

[8] T. Watanabe, S. I. Kimura, and S. Karashima, Philos. Mag. A **49**, 845 (1984).

[9] C. L. Vold and M. E. Glicksman, in *The Nature and Behavior of Grain Boundaries*, edited by H. Hu (Metallurgical Society of AIME, Plenum Press, New York, 1972), pp. 171–183.

[10] F. Inoko, T. Muraga, T. Nakano, and Y. Yoshikawa, T. Interface Sci. **4**, 263 (1997).

[11] S. Divinski, M. Lohmann, C. Herzig, B. Straumal, B. Baretzky, and W. Gust, Phys. Rev. B **71**, 104104 (2005).

[12] J. Luo, V. K. Gupta, D. H. Yoon, and H. M. Meyer, Appl. Phys. Lett. **87**, 231902 (2005).

[13] V. K. Gupta, D. H. Yoon, H. M. Meyer, and J. Lou, Acta Mater. **55**, 3131 (2007).

[14] A. E. Lobkovsky and J. A. Warren, Physica D **164**, 202 (2002).

[15] M. Tang, W. C. Carter, and R. M. Cannon, Phys. Rev. Lett. **97**, 075502 (2006); Phys. Rev. B **73**, 024102 (2006).

[16] Y. Mishin, W. J. Boettinger, J. A. Warren, and G. B. McFadden, Acta Mater. **57**, 3771 (2009).

[17] N. Wang, R. Spatschek, and A. Karma, e-print arXiv:0912.4627.

[18] J. Berry, K. R. Elder, and M. Grant, Phys. Rev. B **77**, 224114 (2008).

[19] J. Mellenthin, A. Karma, and M. Plapp, Phys. Rev. B **78**, 184110 (2008).

[20] J. J. Hoyt, D. Olmsted, S. Jindal, M. Asta and A. Karma, Phys. Rev. E **79**, 020601(R) (2009).

[21] T. Nguyen, P. S. Ho, T. Kwok, C. Nitta, and S. Yip, Phys. Rev. Lett. **57**, 1919 (1986).

[22] P. S. Ho, T. Kwok, T. Nguyen, C. Nitta, and S. Yip, Scr. Metall. **19**, 993 (1985).

[23] G. Ciccotti, M. Guillope, and V. Pontikis, Phys. Rev. B **27**, 5576 (1983).

[24] M. Guillope, G. Ciccotti, and V. Pontikis, Surf. Sci. **144**, 67 (1984).

[25] J. Q. Broughton and G. H. Gilmer, Phys. Rev. Lett. **56**, 2692 (1986).

[26] J. Q. Broughton and G. H. Gilmer, Modell. Simul. Mater. Sci. Eng. **6**, 87 (1998).

[27] J. F. Lutsko, D. Wolf, S. R. Phillpot, and S. Yip, Phys. Rev. B **40**, 2841 (1989).

[28] R. Kikuchi and J. W. Cahn, Phys. Rev. B **21**, 1893 (1980).

[29] A. Suzuki and Y. Mishin, Mater. Sci. Forum **502**, 157 (2005).

[30] G. Besold and O. G. Mouritsen, Comput. Mater. Sci. **18**, 225 (2000).

[31] P. Keblinski, D. Wolf, S. R. Phillpot, and H. Gleiter, Philos. Mag. A **79**, 2735 (1999).

[32] J. Lu and J. A. Szpunar, Interface Sci. **3**, 143 (1995).

[33] P. L. Williams and Y. Mishin, Acta Mater. **57**, 3786 (2009).

[34] S. von Alfthan, K. Kaski, and A. P. Sutton, Phys. Rev. B **76**, 245317 (2007).

[35] M. I. Mendelev, S. Han, D. J. Srolovitz, D. Y. Sun and M. Asta, Philos. Mag. **83**, 3977 (2003) (The potential referred to as "potential 2.").

[36] R. Lipowsky, Phys. Rev. Lett. **57**, 2876 (1986).

[37] D. R. Clarke, J. Am. Ceram. Soc. **70**, 15 (1987).

[38] B. Widom, J. Chem. Phys. **68**, 3878 (1978).

[39] R. Lipowsky and M. E. Fisher, Phys. Rev. B **36**, 2126 (1987).

[40] S. M. Foiles, M. I. Baskes, and M. S. Daw, Phys. Rev. B **33**, 7983 (1986).

[41] J. J. Hoyt, M. Asta, and A. Karma, Mater. Sci. Eng. R. **41**, 121 (2003).

[42] D. L. Olmsted, Acta Mater. **57**, 2793 (2009).

[43] S. J. Plimpton, J. Comput. Phys. **117**, 1 (1995).

[44] S. Melchionna, G. Ciccoti, and B. L. Holian, Mol. Phys. **78**, 533 (1993).

[45] C. L. Kelchner, S. J. Plimpton, and J. C. Hamilton, Phys. Rev. B **58**, 11085 (1998).

[46] J. R. Morris, Phys. Rev. B **66**, 144104 (2002).

[47] B. Dünweg and W. Paul, Int. J. Mod. Phys. C **2**, 817 (1991).